


Article

Cross-Layer Installed Cable-Bracing Inerter System for MDOF Structure Seismic Response Control

Songtao Xue ^{1,2}, Jianfei Kang ¹, Liyu Xie ^{1,*} , Ruifu Zhang ¹  and Xinlei Ban ¹

¹ Department of Disaster Mitigation for Structures, Tongji University, Shanghai 200092, China; xue@tongji.edu.cn (S.X.); 1832540@tongji.edu.cn (J.K.); zhangruifu@tongji.edu.cn (R.Z.); 1610229@tongji.edu.cn (X.B.)

² Department of Architecture, Tohoku Institute of Technology, Sendai 982-8577, Japan

* Correspondence: liyuxie@tongji.edu.cn; Tel.: +86-21-6598-2390

Received: 20 July 2020; Accepted: 22 August 2020; Published: 26 August 2020



Abstract: Inerter-based vibration control systems have been developed rapidly in recent years. However, previous studies mainly focus on the development of new devices and parameter optimization strategies, while ignoring the improvements in the utilization efficiency of the inerter system that the bracing system and novel installation methods may bring. In this paper, a cross-layer installed cable-bracing inerter system (CICBIS) is proposed to improve the utilization efficiency of the inerter system, which can cross more layers and is suitable for shear-type multi-degree-of-freedom (MDOF) structures. A demand-based cable-bracing inerter system (CBIS) design method is developed. The mass enhancement and utilization efficiency improvement of the inerter system caused by the cross-layer installation are quantified through calculating the effective inerter-mass ratio of the CBIS-equipped MDOF structure. A 10-story benchmark structure is used to verify the control performance of the CICBIS and the design method. The analysis results show that the proposed design method can exert the cable-bracing system's adjustability and the damping enhancement of the inerter system. The CICBIS can reduce the total apparent mass and damping coefficient requirements of the inerter systems without increasing the control force. It means that the proposed design method is effective, and the CICBIS has a high efficiency.

Keywords: passive vibration control; inerter system; cross-layer; cable-bracing system; multi-degree-of-freedom structure

1. Introduction

Since the concept of a structural control was proposed [1–3], it has been widely used to improve the performance of buildings under various excitations, especially for those in earthquake-prone areas. In recent years, the introduction of inerters, a novel mechanical element [4], further developed the control strategies. A large number of inerter-based vibration control systems have emerged [5–9].

An inerter is a two-terminal element, generating a resisting force proportional to the acceleration difference between its two ends, which is a significant difference with the traditional one-node mass whose inertial force is dependent on absolute acceleration. The liquid mass pump developed by Kawamata [10] in the 1970s is regarded as the bud of the two-terminal inerter element and was initially utilized as an auxiliary mass to modify the natural frequency of the structure for its high inertial resistance. In 1999, a ball screw viscous damper proposed by Arakaki [11,12], called the rotary damping system, utilized the ball screw mechanism to enhance the damping effect, while the benefits of its mass amplification effect were not used intentionally. Subsequently, researchers found that combing the inerter in series or parallel with springs and damping elements could achieve a better energy dissipation capability. Ikago and his coworkers [5,13,14] proposed a tuned viscous mass damper

(TVMD), which is the first to make full use of its damping enhancement effect and mass amplification effect. These devices, similar to the TVMD, combining the inerter, damping elements, and springs together for vibration control, are called the inerter system [15,16] or an inerter-based damper [17]. Various studies on the topological combinations of the inerter system [18] and their composition parameter optimizations [9,16,19] have been published.

The inerter element with the mass magnification effect can connect the mass of a traditional tuned mass damper to the structure, making the tuned mass damper lightweight and so its performance improves [20–22]. Meanwhile, due to its excellent damping capacity, the inerter system can serve as a damper element substituting the traditional damper in vibration control systems, such as a traditional tuned mass damper [23], and base isolation systems [24–26]. The performance improvements introduced by the inerter element and inerter system have been verified.

Indeed, without being combined with other vibration control systems, taking advantage of the damping enhancement and mass magnification effects, the inerter system still prevails over traditional control strategies in terms of achieving a lightweight and efficient structural control performance. In 2012, Ikago et al. [5] provided a tuning design formula for a single-degree-of-freedom (SDOF) structure equipped with the TVMD based on the fixed-point method and verified the TVMD seismic control effect through shaking table tests. In [27,28], Ikago et al., using sequential quadratic programming, studied the distribution and parameter optimizations of the TVMDs installed on each story of a multiple-degree-of-freedom (MDOF) structure, and further simplified the design by assuming the distribution of the masses of the TVMDs were proportional to the stiffness of each story. In 2014, through a modal analysis and a numerical example, Lazar et al. [6] studied the tuned inerter damper (TID), one of the typical inerter systems, and illustrated that the best installation location is the bottom layer. Wen et al. [29] studied the distributions and parameter optimizations of the TVMD and the TID considering multi-modal seismic control and verified their effectiveness. Pan and Zhang [15,16] studied the closed-form response of SDOF structures equipped with three typical inerter systems, respectively, and provided a demand-based parametric design method. In [19], they found the damping enhancement equation and clarified the damping enhancement effects' fundamental principle.

Besides, some research considering the cost of the inerter systems has been carried out as well. The cost of the inerter system is mainly related to its control force and parameter requirements. In [6], the authors pointed out that due to the inter-story installation scheme, to obtain an identical structural control performance with the tuned mass damper, the apparent mass and damping coefficient requirement of the TID needed to be enlarged, consequently causing the force exerted from the TID on the structure to increase. Considering the potentially increased cost of the inerter system, Taflanidis et al. [7] proposed a trade-off solution. They developed a dual-objective design approach for the structure equipped with a different inerter system, giving Pareto optimality between the structural control performance and the control force of the inerter system. Zhang et al. [30] confirmed that two inerter systems, instead of a single one, installed at the bottom story could reduce the size and control force of the device, thus facilitating the manufacture and improving the structural control performance at the same time. However, using the Pareto optimality to reduce the control force of the inerter system is based on sacrificing the control performance. Utilizing multiple inerter systems, being equipped at each story or concentrated at the bottom layer, to meet various optimization goals, requires many quantities and types of inerter systems, which will still increase the overall cost. Indeed, improving the utilization efficiency of the inerter system is an effective way to reduce its cost.

For improving the utilization efficiency of the inerter system, instead of utilizing the structural shear deformation between consecutive layers, different installation schemes considering the vibration characteristics of the structure have been studied. Asai et al. [31] proposed outrigger TVMDs utilizing the bending deformation instead of the shear deformation of high-rise structures. Ogino and Sumiyama [32] confirmed the high performance of the practical application of the TVMDs installed across three layers using a chevron steel brace in a 37-story building. Additionally, proposing to connect the inerter to a toggle brace, Hwang et al. [33] were the first to use the support with an amplification

effect to enhance the efficiency of the inerter. However, the outrigger TVMD is only suitable for outrigger structures. The chevron steel brace and toggle brace are inevitably bulky due to buckling issues. Besides, it is inconvenient to adjust the displacement transition ratio of the chevron steel brace, which results in different sizes of inerter which are needed to achieve an optimal distribution of the inerter systems.

In contrast, the cable-bracing system has advantages in terms of being lightweight due to its tension-only and adjustability characteristics. Xie et al. [34] proposed a cable-bracing inerter system (CBIS), supporting the inerter system with a simple cable-bracing system, and illustrated its advantages in terms of installation convenience and end constraint release. Sorace and Terenzi [35,36] studied a damped cable system, utilizing prestressed cables to connect fluid viscous spring-dampers and the structure. Utilizing pretensioned rods combined with levers, Aly et al. [37] developed interlayer bracings and outer bracings to connect the magneto-rheological dampers between layers and between the ground and a specific layer, respectively. Kang [38] combined the pretensioned cables with a seesaw member and proposed a cable-bracing seesaw system to support a pair of fluid dampers. The cable-bracing seesaw system connecting the grounded dampers directly to the top story exhibited an excellent damping performance.

Making full use of the characteristics of the CBIS and maximizing its utilization efficiency, in this paper, a cross-layer installed CBIS (CICBIS), able to cross more layers and suitable for shear-type MDOF structures, is proposed. The displacement transition ratios of three typical cable-bracing systems are established first and compared with each other. Deriving the equivalent two-degree-of-freedom system of the MDOF structure equipped with CBIS considering the installation scheme, the effective inerter-mass ratio is defined to quantify the utilization efficiency of the CBIS. Based on the demand-based design, a design flow is proposed for the MDOF equipped with CBISs. A 10-story benchmark model is applied to illustrate the proposed design flow. Two types of CICBISs and inter-layer-installed CBISs (IICBISs) are designed separately. The control performance of the designed CBISs is compared with each other through a frequency-domain and time-domain analysis. Finally, the time history analysis of the displacement of the inerter system and its damping element is carried out to investigate the damping enhancement effect of the designed inerter system.

2. Theoretical Analysis of CBIS

2.1. Basic Concept of the CBIS

The basic concept of the CBIS is to introduce the cable-bracing system into the installation of the inerter system. The tension-only and adjustability characteristics of the cable-bracing system benefit the CBIS to cross layers and unify the inerter size. The inerter system and the cable-bracing system will be discussed separately in the following content. The nomenclature used in this study is shown in Table A1 in the Appendix A.

2.1.1. The Inerter System

The inerter system used in the CBIS described herein is the TVMD, which is first applied in practice [39]. The damping enhancement effect and mass amplification effect of the TVMD have already been verified by researchers [5,15,16,19]. Figure 1 shows the mechanical schematic of the inerter and the TVMD. The resisting force F_{in} of the inerter is proportional to the acceleration difference between its two ends:

$$F_{in} = m_{in}(\ddot{u}_2 - \ddot{u}_1) = m_{in}\ddot{u}_d \quad (1)$$

where u_1 and u_2 are the displacement of the inerter two ends, respectively. The resisting force and acceleration difference ratio m_{in} is the apparent mass [19], having the same unit of the real mass. With the help of different mechanisms, the inerter can achieve an apparent mass much larger than its real mass. The authors of [39] demonstrated an inerter with a ball screw mechanism applied in practice, achieving an apparent mass of 5400 tons with an actual mass of 560 kg.

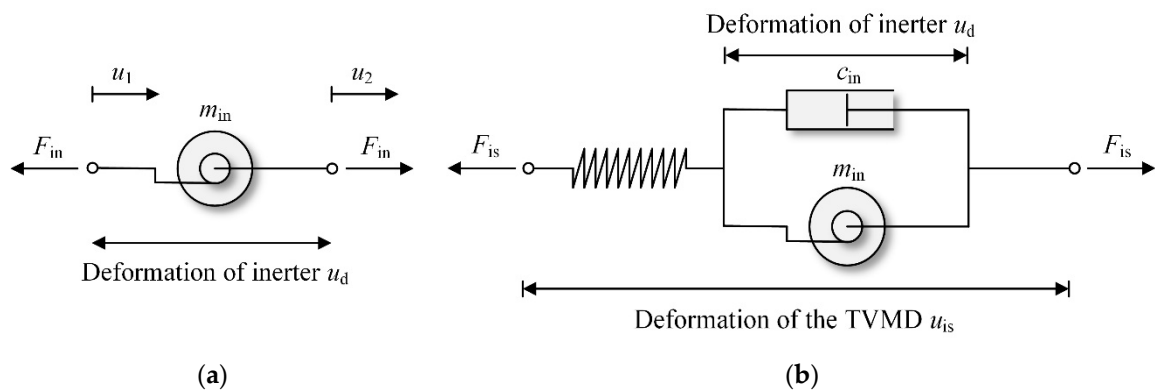


Figure 1. The mechanical schematic of the inerter and the tuned viscous mass damper (TVMD): (a) the inerter; (b) the TVMD.

Assuming the damping coefficient and tuning spring stiffness of the TVMD are c_{in} and k_{in} , respectively, the resisting force F_{is} of the TVMD can be expressed as:

$$F_{is} = k_{in}(u_{is} - u_d) = m_{in}\ddot{u}_d + c_{in}\dot{u}_d \tag{2}$$

where u_{is} and u_d are the displacement differences at two ends of the TVMD and the inerter, respectively.

2.1.2. The Cable-Bracing System

The cable-bracing system proposed in this study consists of a pair of pretensioned diagonal cables and some auxiliary elements (such as the lever, the seesaw system). Figure 2 illustrates three typical forms of cable-bracing systems: (a) simple cable-bracing system [34], (b) cable-bracing lever system [37], and (c) cable-bracing seesaw system [38].

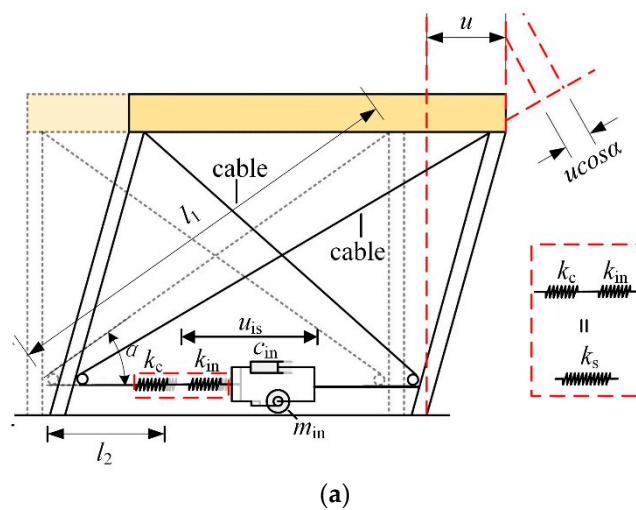


Figure 2. Cont.

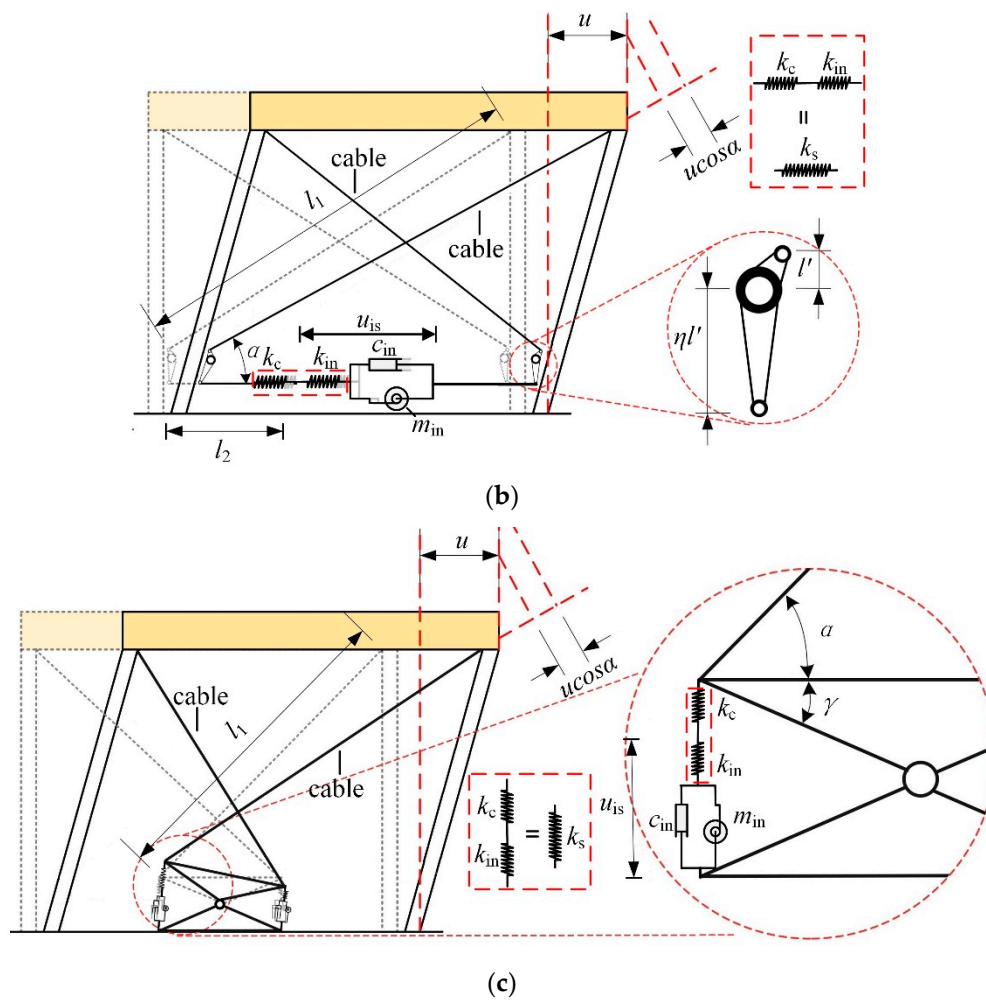


Figure 2. Schematics of different cable-bracing system: (a) simple cable-bracing system; (b) cable-bracing lever system; (c) cable-bracing seesaw system.

In the preliminary design, it is assumed that the stiffness of the auxiliary element is infinite, and the stiffness of the cable-bracing system only depends on the cable stiffness k_c . The cable stiffness k_c can be determined by the following equation:

$$k_c = \frac{E_c A_c}{l_c} \tag{3}$$

where E_c and A_c are the elastic modulus and cross-section area of the cable, respectively; l_c is the cable equivalent length considering the cable-bracing system’s displacement transition mechanism.

Take the cable-bracing systems in Figure 2 as examples, the equivalent length l_c of the simple cable-bracing system equals the total length of its one-side cable. Influenced by the displacement transition mechanism, when calculating the equivalent length l_c of the cable-bracing lever system and cable-bracing seesaw system, their diagonal cable lengths should be weighted according to the principle of stiffness equivalence:

$$l_c = \begin{cases} l_{c1} + l_{c2} & \text{simple cable – bracing system} \\ \eta^2 l_{c1} + l_{c2} & \text{cable – bracing lever system} \\ 2 \left(\frac{\cos(\gamma)}{\sin(\alpha + \gamma)} \right)^2 l_{c1} & \text{cable – bracing seesaw system} \end{cases} \tag{4}$$

where l_{c1} and l_{c2} are one-sided diagonal and horizontal cable lengths, respectively; α , η , γ are the cable installation angle, the lever arm ratio, and the seesaw angle, respectively.

Applying a small amount of pretension on the cable helps the cable maintain a straight line in the static state. Caused by the cable’s tension-only characteristic, the cable’s compression will lead it to slack. Thus, the pair of pretensioned cables are stressed alternately during the seismic motion. Figure 2 shows that the cable of the cable-bracing system is in series with the TVMD’s tuning spring, which can be replaced by the stiffness k_s as a whole:

$$k_s = \frac{k_{in}k_c}{k_{in} + k_c} \tag{5}$$

For simplification, we choose the stiffness k_s as a key parameter in the subsequent discussion. The cable stiffness k_c is determined by the selected cable and Equation (4). Submitting k_s and k_c into Equation (5), the tuning spring stiffness k_{in} can be obtained.

The proportion of the structure displacement transferred to the inerter system displacement can be adjusted through auxiliary elements and the cable-bracing system’s installation angle. It reflects the adjustability of the cable-bracing system. In order to compare cable-bracing systems with each other and unify their motion equations, we define the displacement transition ratio as the ratio β of the inerter system displacement and the horizontal displacement of the structure when ignoring the cable flexibility. Take cable-bracing systems in Figure 2 as examples—for the simple cable-bracing system, the inerter system displacement equals the diagonal cable displacement. The lever or seesaw further increase the diagonal cable displacement transferred to the inerter system for the cable-bracing lever system and cable-bracing seesaw system. Thus, the displacement transition ratios are:

$$\beta = \begin{cases} \cos(\alpha) & \text{simple cable – bracing system} \\ \eta \cos(\alpha) & \text{cable – bracing lever system} \\ \frac{2 \cos(\gamma) \cos(\alpha)}{\sin(\alpha + \gamma)} & \text{cable – bracing seesaw system} \end{cases} \tag{6}$$

Figure 3 presents the variation of the displacement transition ratios concerning the cable installation angle α , in case of the lever arm ratio $\eta = 1, 1.5, 2$, and the seesaw angle $\gamma = 20^\circ, 30^\circ, 40^\circ$. Note that the simple cable-bracing system is a specific form of the cable-bracing lever system, of which the arm ratio equals to one.

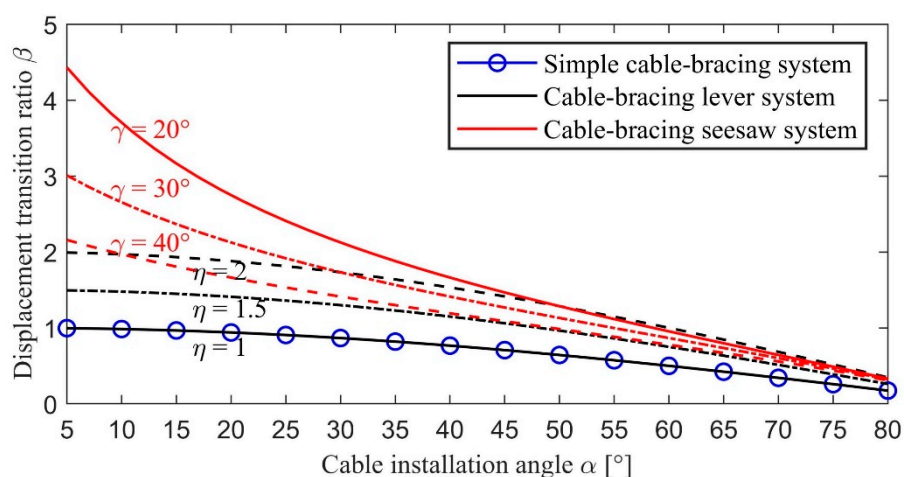


Figure 3. The displacement transition ratio of the cable-bracing inerter system.

From Figure 3, we can see that as the cable installation angle increases, the displacement transition ratios of all cable-bracing systems therein decrease. When the cable installation angle is fixed, the displacement transition ratio of the cable-bracing lever system is proportional to the lever arm,

while the displacement transition ratio of the cable-bracing seesaw system decreases with an increase in the seesaw angle. When the cable installation angle is small, the cable-bracing seesaw system shows a better displacement transition performance than that of the cable-bracing lever system. However, the seesaw cable system’s displacement transition efficiency decreases rapidly with an increase in the cable installation angle. Besides, it is difficult to adjust the displacement transition ratio by changing the seesaw angle, when the cable installation angle is large. In contrast, the cable-bracing lever system’s displacement transition ratio declines relatively slowly and still maintains the adjustability under a large cable installation angle. Thus, we conclude that the cable-bracing seesaw system is suitable for the CBIS with a small cable installation angle and a high demand for the displacement transition ratio, and the cable-bracing lever system is the opposite. It is worth noting that although the cable-bracing system can obtain a higher displacement transition ratio by choosing a larger lever arm or a smaller seesaw angle, this is often accompanied by an increase in the complexity of the cable-bracing system.

For simplicity, during the design procedure, the displacement transition ratio is selected as an optimization variable instead of considering the specific cable-bracing system’s form. The cable installation angle is determined according to specific structure characteristics, such as the story height, column-span, etc. Considering the displacement transition ratio and the cable installation angle, the designers can select the appropriate cable-bracing system.

2.2. Government Equations of the SDOF Structure of a CBIS

As is shown in Figure 4, an SDOF structure, of which the mass, stiffness, damping coefficient are m , k , and c , respectively, is equipped with a CBIS. In Figure 4, a pair of dashed boxes with the connotation β indicate the cable-bracing system, of which the displacement transition ratio equals β .

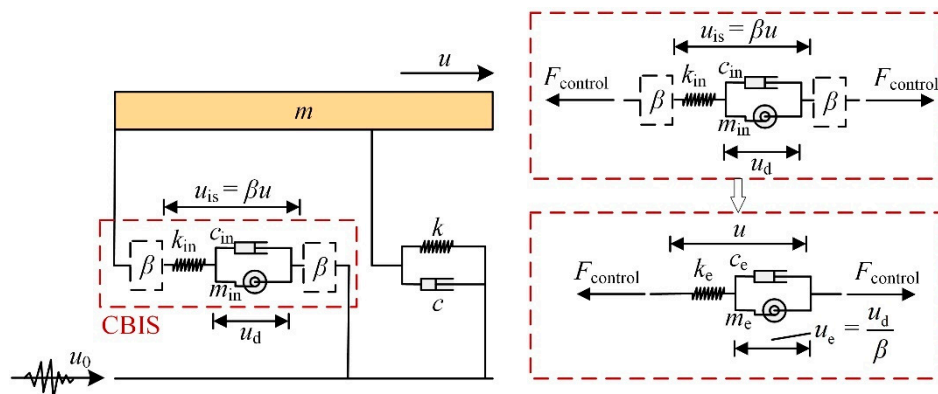


Figure 4. Schematic of the single-degree-of-freedom (SDOF) structure with a cable-bracing inerter system (CBIS).

According to the principle of virtual work, the relationship between the control force applied to the structure, and that of the inerter system is:

$$F_{\text{control}} \cdot 1 = F_{\text{is}} \cdot \beta. \tag{7}$$

where F_{control} and F_{is} are the control force applied to the structure and the force of the inerter system, respectively.

Thus, the governing motion equations of the SDOF structure with CBIS underground motion excitations are:

$$\begin{cases} m\ddot{u} + c\dot{u} + ku + F_{\text{control}} = -m\ddot{u}_0 \\ F_{\text{control}} = \beta F_{\text{is}} = \beta k_s(\beta u - u_d) = \beta(m_{\text{in}}\ddot{u}_d + c_{\text{in}}\dot{u}_d) \end{cases} \tag{8}$$

where u_0 and u are the ground motion displacement, and the displacement of the structure relative to the ground, respectively.

For simplicity, we define an equivalent inerter displacement $u_e = \frac{u_d}{\beta}$, and rearrange Equation (8):

$$\begin{cases} m\ddot{u} + c\dot{u} + ku + F_{\text{control}} = -m\ddot{u}_0 \\ F_{\text{control}} = k_e(u - u_e) = m_e\ddot{u}_e + c_e\dot{u}_e \end{cases} \quad (9)$$

where $m_e = m_{in}\beta^2$, $c_e = c_{in}\beta^2$, $k_e = k_s\beta^2$ are the equivalent apparent mass, equivalent damping coefficient and equivalent stiffness, respectively, as is shown in Figure 4.

2.3. MDOF Structure with the CBISs

The governing motion equations of an uncontrolled MDOF structure's underground motion excitations are:

$$\mathbf{M}_p\ddot{\mathbf{X}}_p + \mathbf{C}_p\dot{\mathbf{X}}_p + \mathbf{K}_p\mathbf{X}_p = -\mathbf{M}_p\mathbf{r}_p\ddot{u}_0 \quad (10)$$

where \mathbf{X}_p is the displacement vector of the MDOF structure relative to the ground; \mathbf{M}_p , \mathbf{K}_p , \mathbf{C}_p denote the mass, stiffness, and damping matrices of the primary structure, respectively; \mathbf{r}_p is the influence coefficient vector.

Let $x_{p,i}$, $m_{p,i}$, $k_{p,i}$, and $c_{p,i}$ denote the relative displacement, mass, stiffness, and damping coefficient of the i^{th} layer of the primary structure, respectively; the matrices in Equation (10) are defined as:

$$\mathbf{X}_p = \{x_{p,1}, x_{p,2}, \dots, x_{p,n}\}^T \quad (11)$$

$$\mathbf{M}_p = \text{diag}\{m_{p,1}, m_{p,2}, \dots, m_{p,n}\} \quad (12)$$

$$\mathbf{K}_p = \mathbf{T}^T \text{diag}(k_{p,1}, k_{p,2}, \dots, k_{p,n}) \mathbf{T} \quad (13)$$

$$\mathbf{C}_p = \mathbf{T}^T \text{diag}(c_{p,1}, c_{p,2}, \dots, c_{p,n}) \mathbf{T} \quad (14)$$

$$\mathbf{r}_p = \{1, 1, \dots, 1\}^T \quad (15)$$

where n is the number of MDOF structure layers; \mathbf{T} is an n -dimension square matrix with 1 in the diagonal and -1 in the first off-diagonal, denoting a transformation matrix defining the relative deformation between consecutive floors.

Similar to the SDOF structure, the motion equations of the MDOF structure with the CBISs can be simplified as:

$$\mathbf{M}\ddot{\mathbf{X}} + \mathbf{C}\dot{\mathbf{X}} + \mathbf{K}\mathbf{X} = -\mathbf{M}\mathbf{r}\ddot{u}_0 \quad (16)$$

where \mathbf{X} denotes the displacement vector of the primary structure and the CBISs; \mathbf{M} , \mathbf{C} , and \mathbf{K} are the mass, damping, and stiffness matrix of the controlled structure, respectively; \mathbf{r} is the influence coefficient vector.

Let $m_{e,i}$, $k_{e,i}$, and $c_{e,i}$ denote the apparent mass, stiffness, and damping coefficient of the i^{th} CBIS, respectively. The matrices in Equation (16) are defined as:

$$\mathbf{X} = \{\mathbf{X}_p^T, \mathbf{X}_e^T\}^T, \text{ where } \mathbf{X}_e = \{x_{e,1}, x_{e,2}, \dots, x_{e,n_d}\}^T \quad (17)$$

$$\mathbf{M} = \begin{bmatrix} \mathbf{M}_p & \\ & \mathbf{M}_e \end{bmatrix}, \text{ where } \mathbf{M}_e = \text{diag}\{m_{e,1}, m_{e,2}, \dots, m_{e,n_d}\} \quad (18)$$

$$\mathbf{C} = \begin{bmatrix} \mathbf{C}_p & \\ & \mathbf{C}_e \end{bmatrix}, \text{ where } \mathbf{C}_e = \text{diag}\{c_{e,1}, c_{e,2}, \dots, c_{e,n_d}\} \quad (19)$$

$$\mathbf{K} = \begin{bmatrix} \mathbf{K}_p + \mathbf{R}_c\mathbf{K}_e\mathbf{R}_c^T & -\mathbf{R}_c\mathbf{K}_e \\ -\mathbf{K}_e^T\mathbf{R}_c^T & \mathbf{K}_e \end{bmatrix}, \text{ where } \mathbf{K}_e = \text{diag}\{k_{e,1}, k_{e,2}, \dots, k_{e,n_d}\} \quad (20)$$

$$\mathbf{r} = \{\mathbf{r}_p^T, 0_{1 \times n_d}\}^T \quad (21)$$

where $x_{e,i}$ denotes the equivalent inerter displacement of the i th CBIS; n_d is the total number of the CBIS; $[\mathbf{R}_c]_{n \times n_d}$ is the installation matrix, denoting the installation location of the CBIS.

Take the j th CBIS installed between the r th and s th layers as an example (as is shown in Figure 5). The installation location of the j th CBIS is represented with the entries in the j th column of \mathbf{R}_c . Only the r th and s th entries of the column are -1 and 1 , representing the j th inerter installation location and the j th cable connection position, respectively, and the rest are all 0. \mathbf{R}_c can express all types of CBIS studied herein ($s - r = 1$ denotes the IICBIS; $s - r > 1$ denotes the CICBIS).

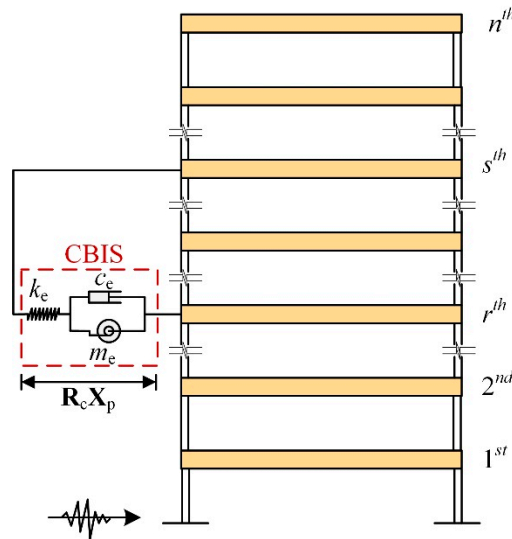


Figure 5. Schematic of an multi-degree-of-freedom (MDOF) structure with a CBIS.

For quantifying the CICBIS advantages, we derived the generalized two-degree-of-freedom equation of the CBIS-equipped MDOF structure based on the Hamiltonian principle and defined its effective inerter-mass ratio. Assuming the vibration shape of an MDOF structure equipped with a CBIS represented by the vector ϕ , the displacement vector \mathbf{X}_p and \mathbf{X}_e can be expressed as:

$$\begin{cases} \mathbf{X}_p = \alpha_p \phi \\ \mathbf{X}_e = \alpha_d \mathbf{R}_c^T \phi \end{cases} \quad (22)$$

where α_p and α_d are generalized coordinates of the primary structure and the inerter, respectively.

Therefore, the kinetic energy E_T , strain energy E_U , and dissipated energy E_D of the CBIS-equipped MDOF structure are:

$$\begin{cases} E_T = \frac{1}{2} \dot{\alpha}_p^2 \phi^T \mathbf{M}_p \phi + \frac{1}{2} \dot{\alpha}_d^2 \phi^T \mathbf{R}_c \mathbf{M}_e \mathbf{R}_c^T \phi \\ E_U = \frac{1}{2} \alpha_p^2 \phi^T \mathbf{K}_p \phi + \frac{1}{2} (\alpha_p - \alpha_d)^2 \phi^T \mathbf{R}_c \mathbf{K}_e \mathbf{R}_c^T \phi \\ E_D = \frac{1}{2} \dot{\alpha}_p^2 \phi^T \mathbf{C}_p \phi + \frac{1}{2} \dot{\alpha}_d^2 \phi^T \mathbf{R}_c \mathbf{C}_e \mathbf{R}_c^T \phi \end{cases} \quad (23)$$

Assuming $L = E_T - E_U$, the Euler–Lagrange equations are:

$$\begin{cases} \frac{d}{dt} \left(\frac{\partial L}{\partial \dot{\alpha}_p} \right) - \frac{\partial L}{\partial \alpha_p} + \frac{\partial E_D}{\partial \dot{\alpha}_p} = 0 \\ \frac{d}{dt} \left(\frac{\partial L}{\partial \dot{\alpha}_d} \right) - \frac{\partial L}{\partial \alpha_d} + \frac{\partial E_D}{\partial \dot{\alpha}_d} = 0 \end{cases} \quad (24)$$

Substituting Equation (23) into Equation (24) gives:

$$\begin{cases} \phi^T \mathbf{M}_p \phi \ddot{\alpha}_p + \phi^T \mathbf{C}_p \phi \dot{\alpha}_p + \phi^T \mathbf{K}_p \phi \alpha_p + \phi^T \mathbf{R}_c \mathbf{K}_e \mathbf{R}_c^T \phi (\alpha_p - \alpha_d) = 0 \\ \phi^T \mathbf{R}_c \mathbf{M}_e \mathbf{R}_c^T \phi \ddot{\alpha}_d + \phi^T \mathbf{R}_c \mathbf{C}_e \mathbf{R}_c^T \phi \dot{\alpha}_d + \phi^T \mathbf{R}_c \mathbf{K}_e \mathbf{R}_c^T \phi (\alpha_d - \alpha_p) = 0 \end{cases} \quad (25)$$

Comparing Equation (25) with Equation (9), the generalized mass M_p of the primary structure and the generalized apparent mass M_d of the CBIS can be expressed as:

$$\begin{cases} M_p = \phi^T \mathbf{M}_p \phi \\ M_d = \phi^T \mathbf{R}_c \mathbf{M}_e \mathbf{R}_c^T \phi \end{cases} \quad (26)$$

The performance of the tuned inerter systems is positively related to their mass ratio [5]. In the generalized two-degree-of-freedom equation, the effective inerter-mass ratio μ is defined as:

$$\mu = \frac{M_d}{M_p} = \frac{\phi^T \mathbf{R}_c \mathbf{M}_e \mathbf{R}_c^T \phi}{\phi^T \mathbf{M}_p \phi} \quad (27)$$

Note that the installation location vector \mathbf{R}_c only affects the generalized apparent mass of the CBIS, but has no effect on the generalized mass of the primary structure. When the cross-layer installation, expressed by the installation location vector \mathbf{R}_c , leads the displacement between the layers of the structure to be superimposed, the effective inerter-mass ratio μ will be amplified, which means the utilization efficiency of the inerter system is improved. The design example illustrated in Section 4 has verified this amplification effect numerically.

3. Optimum Seismic Control of an MDOF System with CBISs

3.1. Evaluation of the Seismic Response

The state-space approach [40] is employed here to evaluate the seismic responses on their high efficiencies. The seismic input action is simulated as a Kanai–Tajimi filtered white noise [41]:

$$S_g(\omega) = \frac{\omega_g^4 + 4\zeta_g^2 \omega^2 \omega_g^2}{(\omega_g^2 - \omega^2)^2 + 4\zeta_g^2 \omega^2 \omega_g^2} S_0 \quad (28)$$

where ω_g, ζ_g are the frequency and damping properties of the supporting ground, respectively; S_0 is the intensity of the white noise excitation at the bedrock, associated with the ground motion acceleration \ddot{u}_0 :

$$S_0 = \frac{0.141 \zeta_g \ddot{u}_0^2}{\omega_g \sqrt{1 + 4\zeta_g^2}} \quad (29)$$

Rewriting the Kanai–Tajimi power spectrum (Equation (28)) into the form of state-space equations gives:

$$\begin{cases} \dot{x}_q = \mathbf{A}_q x_q + \mathbf{E}_q w \\ \ddot{x}_g = \mathbf{C}_q x_q \end{cases} \quad (30)$$

where $\mathbf{A}_q = \begin{bmatrix} 0 & 1 \\ -\omega_g^2 & -2\zeta_g \omega_g \end{bmatrix}$, $\mathbf{C}_q = \sqrt{2\pi S_0} [-\omega_g^2 - 2\zeta_g \omega_g]$, $\mathbf{E}_q = \begin{bmatrix} 0 \\ 1 \end{bmatrix}$.

Let the $x_R = \{\mathbf{X}^T, \dot{\mathbf{X}}^T\}^T$. Rewriting Equation (16) with a state-space form gives:

$$\dot{x}_R = \mathbf{A}_R x_R + \mathbf{E}_R w \quad (31)$$

where $x_R = \{\mathbf{X}^T, \dot{\mathbf{X}}^T\}^T$, $\mathbf{A}_R = \begin{bmatrix} 0_{(n+n_d) \times (n+n_d)} & \mathbf{I}_{(n+n_d) \times (n+n_d)} \\ -\mathbf{M}^{-1} \mathbf{K} & -\mathbf{M}^{-1} \mathbf{C} \end{bmatrix}$, $\mathbf{E}_R = \begin{bmatrix} 0_{1 \times (n+n_d)} & -\mathbf{r}^T \end{bmatrix}^T$, and w denotes the white noise input.

Combining Equations (31) and (30), extended state-space equations considering the Kanai–Tajimi power spectrum are obtained:

$$\begin{cases} \dot{x}_s = \mathbf{A}_s x_s + \mathbf{E}_s w \\ z = \mathbf{C}_s x_s \end{cases} \quad (32)$$

where $x_s = \begin{Bmatrix} x_R \\ x_q \end{Bmatrix}$, $\mathbf{A}_s = \begin{bmatrix} \mathbf{A}_R & \mathbf{E}_R \mathbf{C}_q \\ \mathbf{0}_{2 \times (2n+2n_d)} & \mathbf{A}_q \end{bmatrix}$, $\mathbf{E}_s = \begin{bmatrix} \mathbf{0}_{(2n+2n_d) \times 1} \\ \mathbf{E}_q \end{bmatrix}$; the output matrix \mathbf{C}_s , used to calculate the output vector z which includes the inter-story drifts of the structure and forces of the CBISs, is defined as:

$$\mathbf{C}_s = \begin{bmatrix} \mathbf{T} & \mathbf{0}_{n \times (2n+2n_d+2)} \\ -\mathbf{K}_e^T \mathbf{R}_c^T & \mathbf{K}_e \quad \mathbf{0}_{n_d \times (n+n_d+2)} \end{bmatrix} \quad (33)$$

The direct stochastic analysis method [40] ensures that the covariance matrix of the output vector z is:

$$\mathbf{K}_{zz} = \mathbf{C}_s \mathbf{P} \mathbf{C}_s^T \quad (34)$$

where the state covariance matrix \mathbf{P} is the solution of the following Lyapunov equation:

$$\mathbf{A}_s \mathbf{P} + \mathbf{P} \mathbf{A}_s^T + \mathbf{E}_s \mathbf{E}_s^T = 0 \quad (35)$$

Note that the diagonal terms of the covariance matrix \mathbf{K}_{zz} contain all the response information on the inter-story drifts of the structure and forces of the CBISs. The root of first n diagonal terms are the root mean square (RMS) structural responses σ_u of each layer, and the root of the remaining items are the RMS control forces σ_F of each CBIS.

3.2. Design Formulation and Procedure

The design of the CBISs used to attenuate the MDOF structure seismic response includes the total number determination, the placement design, and the parameter optimizations. The total number and placement of the CBISs can be predetermined through an initial analysis of the structure and by considering the building facade limitations. Typically, considering the high efficiency of the CICBISs, there is no need to install them at each layer. The demand-based design method is adopted herein to optimize the parameters of the CBISs to ensure the vibration performance of the structure while reducing the cost of manufacturing and installing the CBISs.

For intuitively expressing the optimization process, the design variables representing the CBISs are adopted and defined as the following:

$$y = \{m_d, c_d, \omega_r, \beta_1, \beta_2, \dots, \beta_{n_d}\} \quad (36)$$

where m_d , c_d are the designed apparent mass, and the designed damping coefficient of the inerter system, respectively; β_i denotes the displacement transition ratio of the i th cable-bracing systems and n_d denotes the total number of CBISs; ω_r is the frequency of the CBIS defined as:

$$\omega_r = \sqrt{\frac{k_d}{m_d}} \quad (37)$$

where k_d denotes the designed stiffness of the CBISs.

The equivalent parameters of each CBIS can be calculated by the following equations:

$$\begin{cases} m_{e,i} = m_d \cdot \beta_i^2 \\ k_{e,i} = m_d \cdot \omega_r^2 \cdot \beta_i^2 \\ c_{e,i} = c_d \cdot \beta_i^2 \end{cases} \quad i = 1, \dots, n_d \quad (38)$$

It is worth noting that the displacement transition ratios reflect the proportional relationship between each CBIS, and their specific value can be determined by presetting the designed apparent mass m_d .

The performance of the CBIS in terms of attenuating the MDOF structure seismic response is represented by the drift reduction ratio J_p :

$$J_p = \max_{i=1}^n \left[\frac{\sigma_u(i)/h_i}{\theta_{0\max}} \right] \tag{39}$$

where $\sigma_u(i)$ denotes the i th RMS story drift of the controlled structure; h_i denotes the i th floor height of the structure; $\theta_{0\max}$ denotes the maximum RMS story drift ratio of the uncontrolled structure.

Since the materials' strength required for the manufacturing of the inerter system and the strength of the anchor nodes are positively related to the control force [7,15,16], the RMS control force of a CBIS is herein selected as its cost index. Because the inerter system of each CBIS is the same, the cost index of installing n_d CBISs J_F can be estimated as:

$$J_F = n_d \max_{i=1}^{n_d} \{\sigma_F(i)\} \tag{40}$$

where $\sigma_F(i)$ is the RMS control force of the i th CBIS.

The increase in the connection stiffness may achieve a better control effect, while it comes at the cost of tuning effects and tremendously increases the apparent mass and damping coefficient requirements of the inerter system. We limit the frequency of the CBIS as follows to enhance the tuning effect and get a reasonable solution, as Ikago et al. did in [27]:

$$\omega_r = \frac{1}{\sqrt{1 - {}_1\mu}} {}_1\omega_0 \tag{41}$$

where ${}_1\omega_0$ denotes the natural frequency of the uncontrolled structure; ${}_1\mu$ is the effective inerter-mass ratio, which can be obtained by submitting the equivalent apparent mass matrix \mathbf{M}_e , \mathbf{R}_c represents the location matrix of CBISs, and the first-order modal vector ${}_1\phi$ into Equation (27).

Thus, the demand-based optimization for the CBISs is formulated:

$$\begin{aligned} &\text{find} && y = \{m_d, c_d, \omega_r, \beta_1, \beta_2, \dots, \beta_{n_d}\} \\ &\text{to minimize} && J_F(y) \\ &\text{subject to} && \begin{cases} J_p(y) \leq J_{\text{target}} \\ \omega_r = \frac{1}{\sqrt{1 - {}_1\mu}} {}_1\omega_0 \\ m_d = m_{\text{design}} \end{cases} \end{aligned} \tag{42}$$

where J_{target} is the target drift reduction ratio determined by the performance demands [15,16]. m_{design} is the predetermined designed apparent mass, determined by the inerter model.

Finally, suitable cable-bracing systems are selected considering their structural characteristics and the displacement transition ratios. The design flowchart is shown in Figure 6.

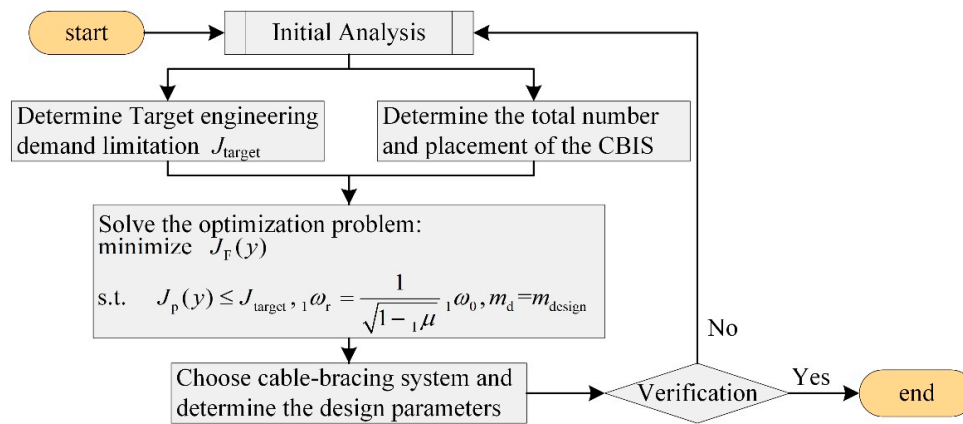


Figure 6. Design flowchart.

4. An Illustrative Design Example

4.1. Analysis Model

The benchmark structure used in this study is a 10-story building proposed by the Japan Society for Seismic Isolation [42], the detailed information of which is shown in Figure 7 and Table 1.

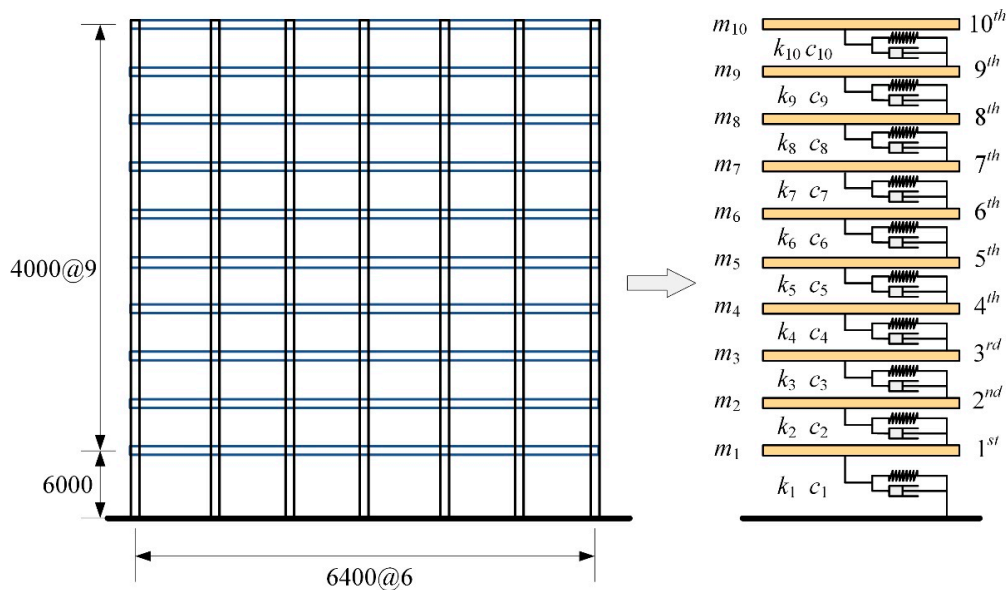


Figure 7. 10-story benchmark structure.

Table 1. Characteristics of the benchmark building.

Story	Mass m_i ($\times 10^3$ kg)	Stiffness k_i (kN/m)	Height (m)
10	875.4	158,550	4
9	649.5	180,110	4
8	656.2	220,250	4
7	660.2	244,790	4
6	667.2	291,890	4
5	670.1	306,160	4
4	675.7	328,260	4
3	680.0	383,020	4
2	681.6	383,550	4
1	699.9	279,960	6

By calculating the effective inerter-mass ratios of a CBIS installed in the structure, the influence of the installation location and cross-layer installation method on the utilization efficiency of the CBIS is determined first. The effective inerter-mass ratios of the IICBISs and CICBISs (cross-two-layers and cross-three-layers) installed in all possible locations are illustrated in Figure 8a, respectively. In Figure 8a, the horizontal axis is the effective inerter-mass ratio normalized by $\frac{m_e}{\phi^T M_{p1} \phi}$, representing the utilization efficiency of the CBIS, and the vertical axis is the inerter installed location. Figure 8a shows that since the height of the bottom layer of the benchmark structure is higher than the other layers, the bottom displacement of the structure is more significant and results in the CBIS reaching the highest utilization efficiency when installed at the bottom. Except for the bottom and top layers, the efficiency of CBISs installed on other layers is similar. Comparing the CBISs installed on the same layer, we can conclude that the normalized inerter-mass ratios of the cross two-layer and cross three-layer-installed CBISs are at least 2.78 and 5.74 times larger than those of the IICBIS, respectively. Considering the possible number of layers that the CBIS can cross, the bottom layer, the second layer, and the third layer-installed CBISs are illustrated in Figure 8b. Note that with the increase in the number of crossed layers, the normalized inerter-mass ratio improves significantly, and the CBIS-installation crossing all layers has the highest utilization efficiency.

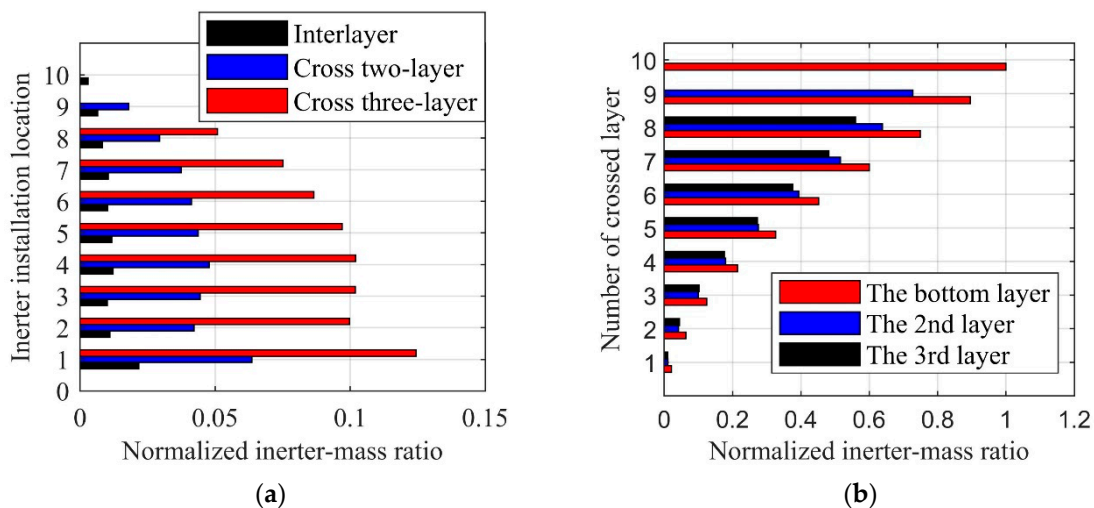


Figure 8. Illustration of the modal inerter-mass ratios: (a) the influence of installation location; (b) the influence of the crossed layer number.

4.2. Design of the CBISs

According to the above analysis, we can conclude that installing the CBIS crossing all layers is the most efficient installation method. However, the more layers crossed, the higher the requirements on the construction and maintenance of the CBIS, and sometimes the number of layers that the CBIS can cross is limited by the building facade requirements. Since these engineering factors are difficult to quantify, we recommend and analyze the cross-all-layers and cross-three-layers installed CBISs as two possible selections (CASE A and CASE B) showed in Figure 9. CASE A and CASE B represent the most efficient installation method and an easier-to-implement installation method, respectively. The vertical distribution of the CICBISs in CASE B is uniform to ensure a reasonable control force distribution. Thus, the total number of CICBISs is selected to be three, and the inerter installation locations are selected as the bottom, third, and sixth layer. Meantime, another design scheme, installing the IICBISs layer by layer on the benchmark structure, is illustrated as well to compare with the CICBISs, as CASE C showed in Figure 9, the IICBISs are divided into three groups, thereby limiting the types of cable-bracing systems to ensure engineering practice.

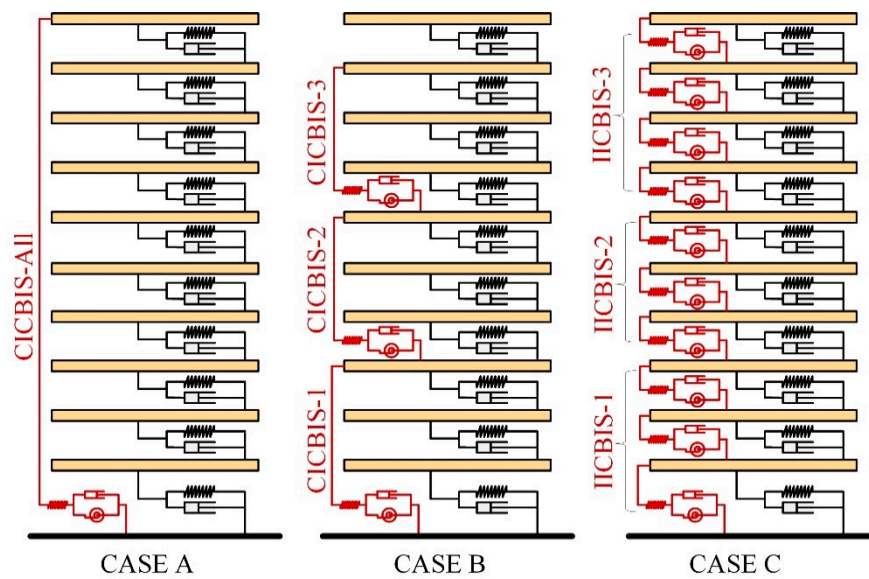


Figure 9. Schematic of the benchmark building with the cable-bracing inerter systems (CICBISs) and inter-layer-installed CBISs (IICBISs).

The optimization problems for CASE A, CASE B, and CASE C in Figure 9 can be expressed as:

$$\begin{aligned}
 & \text{find} && y = \{m_d, c_d, \omega_r, \beta_1, \beta_2, \dots, \beta_{n_d}\} \\
 & \text{to minimize} && J_F(y) \\
 & \text{subject to} && \begin{cases} J_p(y) \leq J_{\text{target}} \\ \omega_r = \frac{1}{\sqrt{1-\mu}} \omega_0 \\ m_d = m_{\text{design}} \end{cases} \quad (43)
 \end{aligned}$$

where $J_{\text{target}} = 0.5$ determined by the initial analysis and the performance requirements of the primary structure. An inerter with the apparent mass $m_{\text{design}} = 1 \times 10^6 \text{ kg}$ is utilized herein, which can be achieved with an actual mass lower than 150 kg, using the same mass-amplifying mechanism of the inerter mentioned in [39].

The parameters of the Kanai–Tajimi power spectrum used to simulate the seismic excitation are selected as $\omega_g = 4\pi \text{ rad/s}$, $\zeta_g = 0.6$, which is suggested by Kanai [41] for the firm ground.

Table 2 shows the optimal results of CASE A, CASE B, and CASE C obtained using a numerical optimization. Since the unified designed apparent mass is predetermined as $1 \times 10^6 \text{ kg}$, the utilization efficiency of the CICBISs and IICBISs is reflected by the displacement transition ratios. It was found that the average displacement transition ratios of the cross-all-layers and cross-three-layers installed CBISs are about 30.0% and 57.2% of the IICBISs', reflecting the high efficiency of the CICBIS. It is said that when using the cable-bracing system with similar transfer ratios, the designed apparent mass and designed damping coefficient of the CICBIS are much smaller than those of the IICBIS. Furthermore, as the number of the CICBISs used in CASE A and CASE B is smaller than that of the IICBISs in CASE C, the total apparent mass and damping coefficient requirements of the CICBISs are reduced compared with the IICBISs. According to the optimal results shown in Table 2, we can know that the total apparent mass and damping coefficient requirements of cross-all-layers installed CBIS are about 10.0% and 7.5% of the IICBIS's, respectively. The total apparent mass and damping coefficient requirements of the cross-three-layers installed CBISs are reduced to about 33.3% and 27.8% of the IICBIS's, respectively. In fact, the IICBISs in CASE C can be replaced by the traditional TVMDs as well, which have been studied in [27,28]. For achieving the same control effect of the IICBISs, the apparent mass and damping coefficient requirements of each TVMDs are different, listed in Table 2 as well.

Compared with traditional TVMDs, the CBISs show the advantages of a small apparent mass and few damping coefficient requirements.

Table 2. Optimal results of CASE A, CASE B, CASE C.

		m_d (kg)	c_d (kN/m/s)	ω_r	β	k_d (kN/m)
CASE A	CICBIS-All	1,000,000	1605.899	3.259	0.508	10,620.172
CASE B	CICBIS-1				0.909	
	CICBIS-2	1,000,000	1970.397	3.270	0.964	10,695.612
	CICBIS-3				1.040	
CASE C	IICBIS-1				1.535	
	IICBIS-2	1,000,000	2129.588	3.281	1.799	10,766.132
	IICBIS-3				1.754	
	TVMD-1	2,354,898	5014.963	3.281	1.000	25,353.142
	TVMD-2	3,234,898	6889.000	3.281	1.000	34,827.336
	TVMD-3	3,078,151	6555.193	3.281	1.000	33,139.778

In the above design of the CBISs equipped benchmark building, the designed displacement transition ratios are at a relatively low level, and under the premise of making full use of the width of the benchmark building, the cable installation angle ranges from 5.959° to 46.009°. Thus, the cable-bracing lever system is chosen herein. Table 3 lists the design parameters of the cable-bracing lever systems for CASE A, CASE B, and CASE C.

Table 3. Design parameters of the cable-bracing system.

	α (°)	η	β
CICBIS-All	46.009	1.116	0.508
CICBIS-1	20.054	0.968	0.909
CICBIS-2	17.361	1.010	0.964
CICBIS-3	17.361	1.090	1.040
IICBIS-1	5.959 (8.881 ¹)	1.543 (1.554 ¹)	1.535
IICBIS-2	5.959	1.809	1.799
IICBIS-3	5.959	1.764	1.754

¹ The bottom layer parameters.

4.3. Effectiveness of the CICBISs

First, the performance of the CICBISs in terms of attenuating the structure response under the harmonic excitation is analyzed from the perspective of the displacement frequency response functions (FRFs). Taking the fourth layer’s inter-layer drift FRFs, where the maximum inter-layer drift occurs, and the top layer’s absolute displacement FRFs as examples, the FRFs, as is shown in Figure 10, are normalized by the uncontrolled peak response and the black dash line is the FRFs of the uncontrolled structure. The fourth layer FRF curves show that the damping effect of CASE A, CASE B, and CASE C on the first-order response is significant, and their curves almost coincide. It means the CICBISs and IICBISs have a similar control effectiveness on the maximum inter-layer drift layer. The top layer absolute displacement FRF curves show that the structure response is mainly controlled by the first-order modal, i.e., whether the CICBISs or IICBISs can effectively control the overall displacement of the structure. The cross-all-layers installed CBIS can accurately control the first-order modal response without affecting other modes.

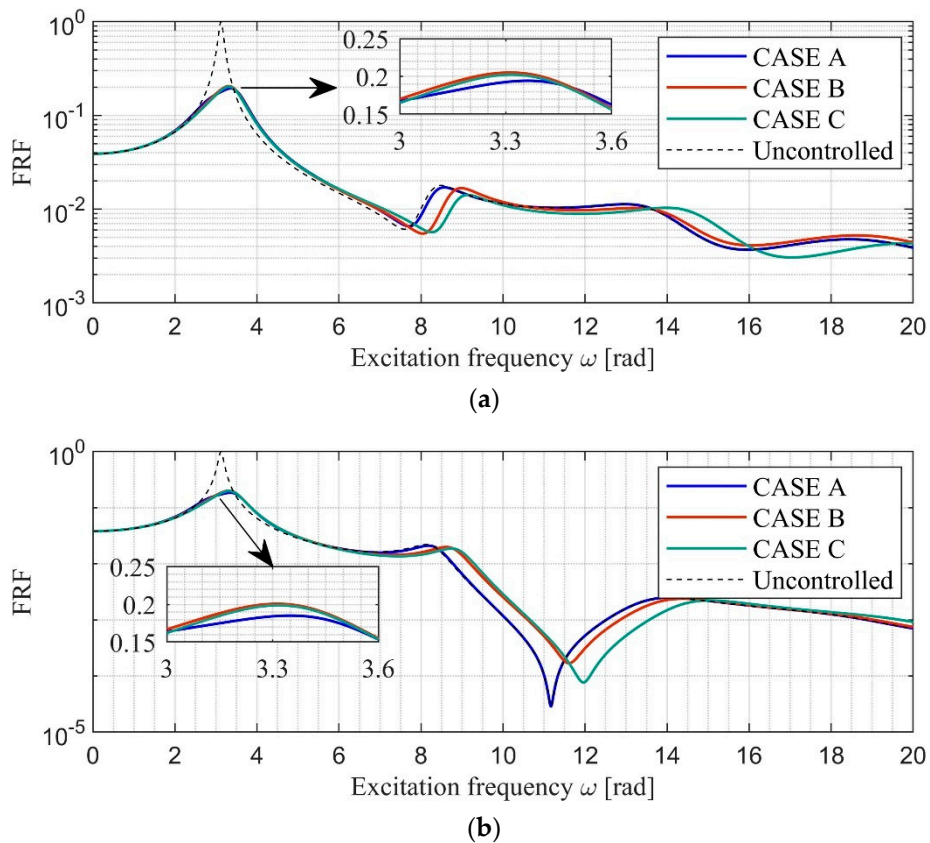


Figure 10. The displacement frequency response functions (FRFs) of CASE A, CASE B, and CASE C: (a) the fourth layer inter-layer drift; (b) the top layer displacement.

Furthermore, Figure 11 shows the RMS responses of the controlled and uncontrolled structures under the stochastic excitation proposed for optimization, where the black dash line is the uncontrolled structure response and the red dash line is the target drift limitation. The RMS inter-layer drift angles in Figure 11a show that both the designed CICBISs and IICBISs have reached the target drift reduction ratio $J_{target} = 0.5$. Consistent with the conclusions reflected in the FRF curves, CASE A, CASE B, and CASE C have almost the same control effect on the structure displacement, except for a slightly difference in the top layer inter-layer drift angle. It is caused by the lack of control device in CASE B. From the RMS control forces of the CICBISs and IICBISs, shown in Figure 11b, it can be concluded that the cross-layer installation will not increase the control force. Table 4 shows the cost index J_F of each design case. It can be seen that the cost indexes of CASE A and CASE B are about 8.2% and 26.3% of CASE C's, respectively, which is mainly caused by the reduced number of the inerter systems used in CASE A and CASE B.

Table 4. The cost index J_F of CASE A, CASE B and CASE C.

	CASE A	CASE B	CASE C
cost index J_F (kN)	718.234	2299.150	8727.719

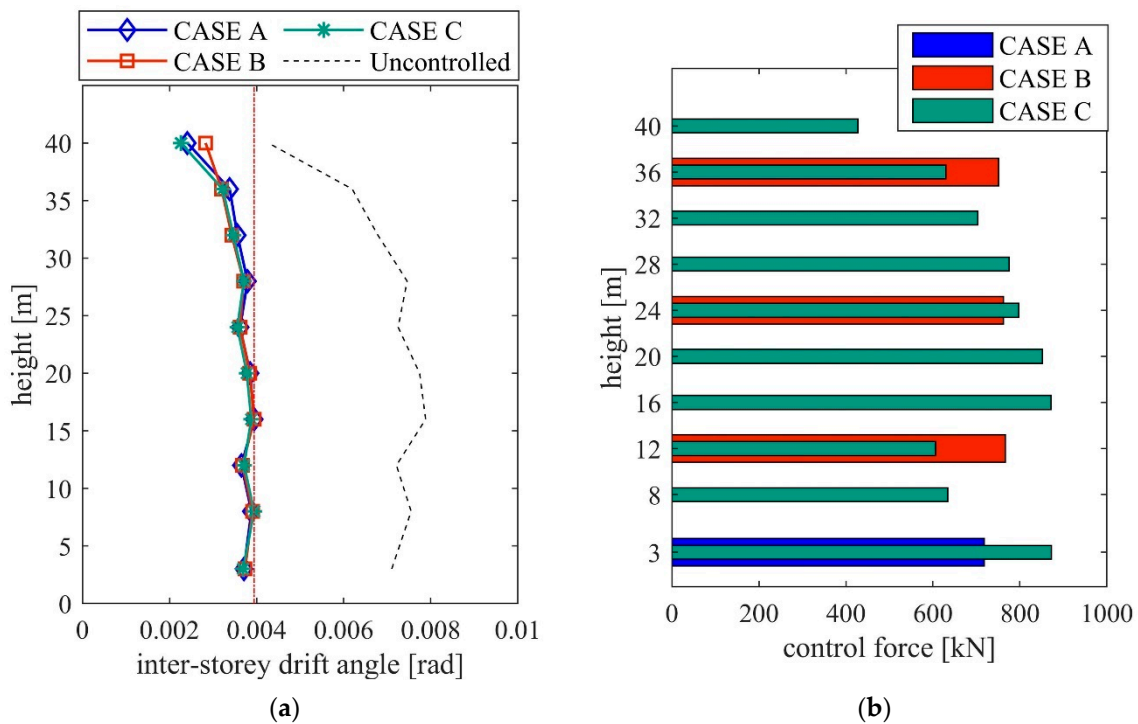


Figure 11. The root mean square (RMS) inter-story drift angle and the RMS control forces: (a) RMS inter-layer drift angles; (b) RMS control forces

Hence, the seismic control effectiveness is investigated herein with a time history analysis. An artificial accelerogram and three recorded earthquake accelerograms, of which the peak accelerations are scaled to be 0.1 g, are employed to conduct the time history analysis. The artificial accelerogram is the BCJ-L2, provided by the Building Center of Japan. The recorded earthquake accelerograms extracted from the Pacific Earthquake Engineering Research Center database (<http://peer.berkeley.edu/nga>) are the Kobe accelerogram (1995), the Chi-chi accelerogram (1999), and the El Centro accelerogram (1940). Figure 12 shows the time history displacement responses of the fourth layer, where the black dash line is the uncontrolled structure response. The drift reduction ratio J_p of each seismic accelerogram is calculated based on the time history responses and is listed in Table 5. All drift reduction ratios are lower than the target drift reduction ratio $J_{target} = 0.5$. CASE A, CASE B, and CASE C show almost the same control effects.

Table 5. Normalized maximum controlled structural drift ratios.

Title 1	BCJ-L2 Artificial Accelerogram	Kobe Accelerogram	Chi-chi Accelerogram	El Centro Accelerogram
CASE A	0.4714	0.4081	0.4906	0.4416
CASE B	0.4690	0.4182	0.4953	0.4469
CASE C	0.4600	0.4111	0.4874	0.4393

Figure 13 shows the deformation of the bottom layer CBIS and its damping element in CASE A, CASE B, and CASE C, with the BCJ-L2 artificial accelerogram as the excitation. It shows that the design method proposed in Section 3.2 ensures the damping enhancement effect of the inerter system, which means the deformation of the damping element in the inerter system is enlarged compared with traditional damper. As is mentioned in [19], the damping deformation enhancement factor, defined as the ratio of RMS deformation of the damping element to that of the inerter system, represents the degree of the damping enhancement effect. The enhancement factors of the CICBIS-A11, CICBIS-1, and IICBIS-1 showed in Figure 13 are 1.7764, 1.506, and 1.399, respectively. The better damping

enhancement effect partly explains the smaller damping requirements of the CICBISs compared to the IICBISs, as is shown in Table 2.

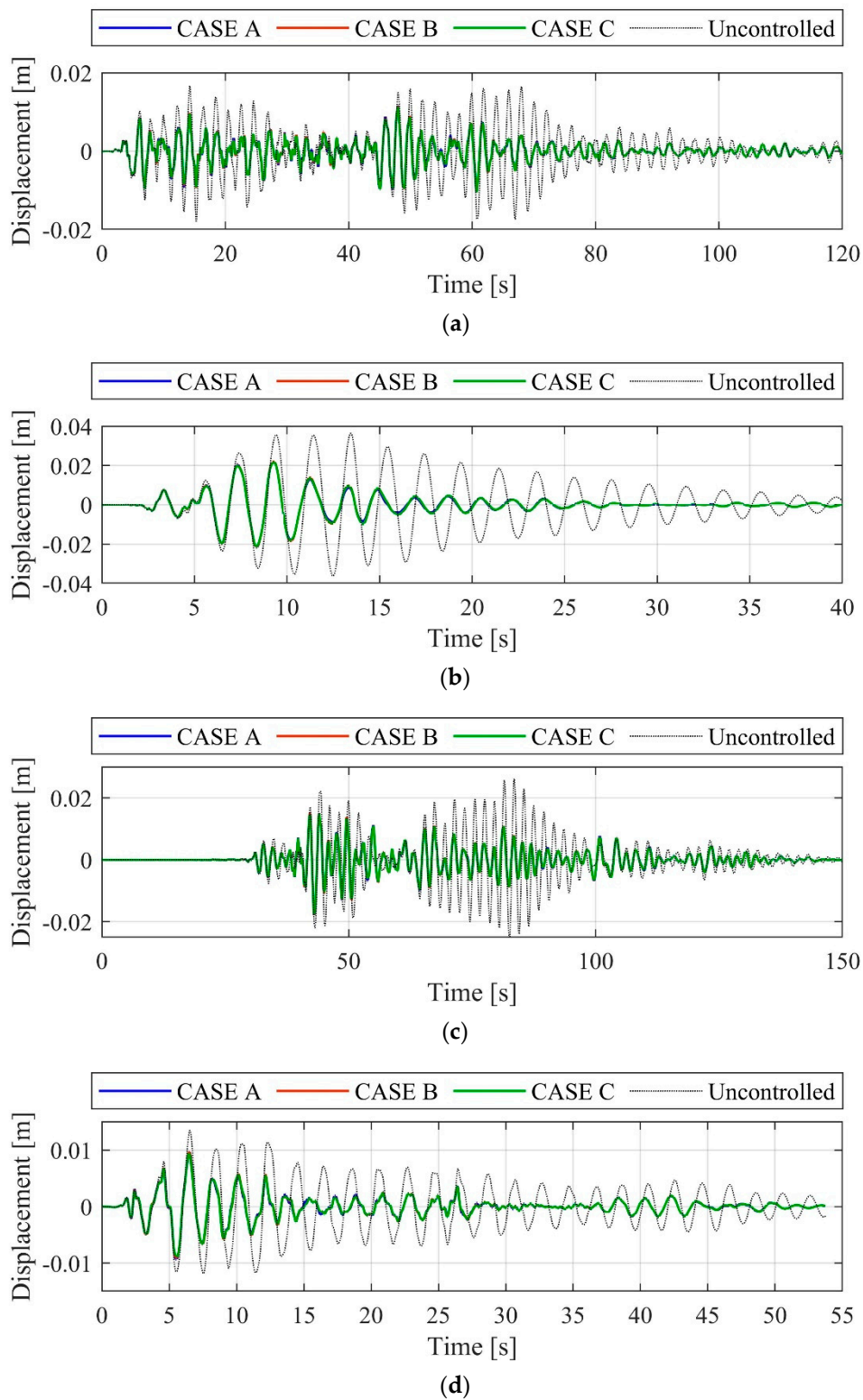


Figure 12. Displacement responses of the fourth layer: (a) BCJ-L2 artificial accelerogram; (b) Kobe accelerogram; (c) Chi-chi accelerogram; (d) El Centro accelerogram.

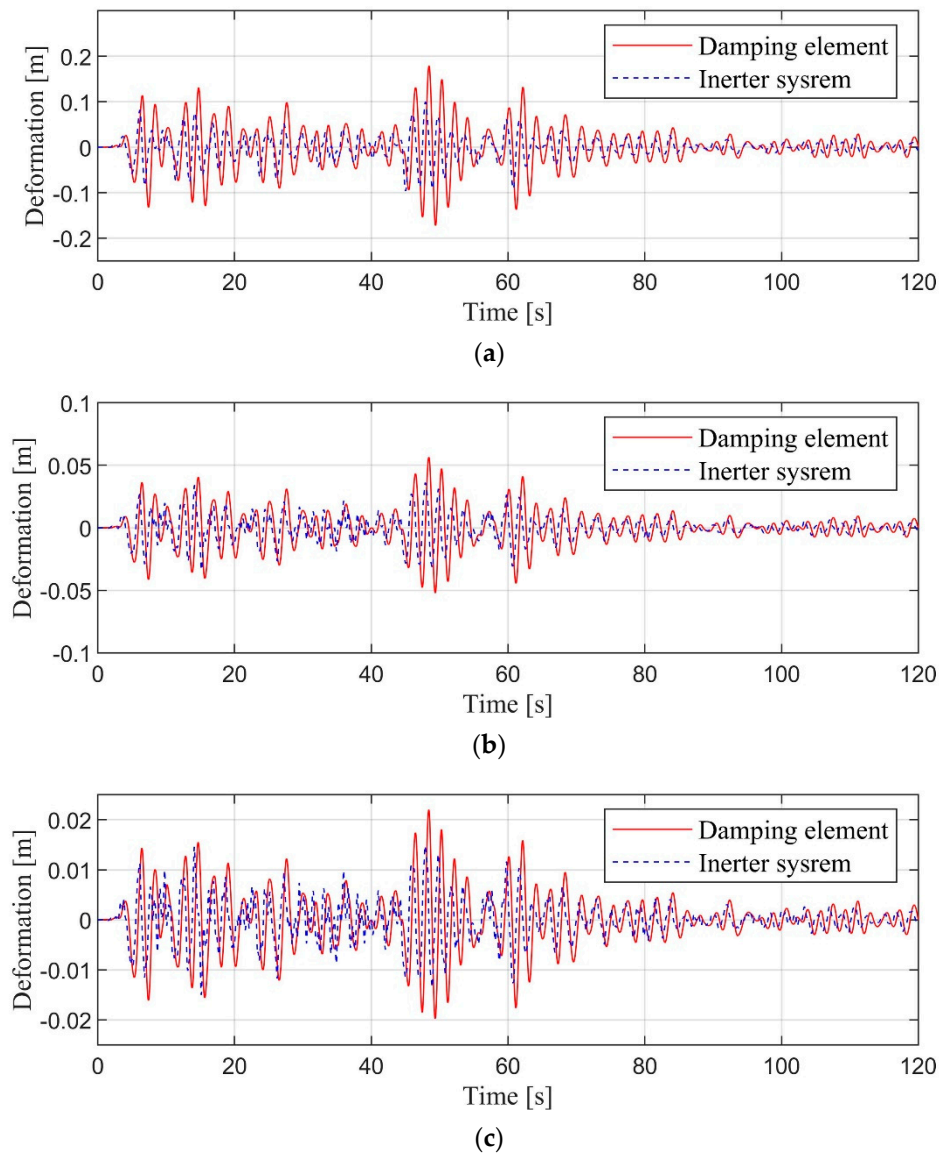


Figure 13. The displacement responses of the bottom layer CBIS: (a) CICBIS-A11; (b) CICBIS-1; (c) IICBIS-1.

5. Conclusions

In this paper, we studied the CBIS and proposed the CICBIS to improve the utilization efficiency of the inerter system for shear-type MDOF structure seismic response control. A demand-based CBIS design method is developed as well. The main contributions of this paper are summarized as follows:

- The ability of the CICBIS to reduce the total apparent mass and damping coefficient requirements of the inerter systems without increasing the control force has been confirmed. Thus, the CICBIS with a high efficiency provides a feasible solution to attenuate the in-built or existing building's seismic response.
- The demand-based CBIS design method proposed herein can exert the damping enhancement of the inerter system and the adjustability of the cable-bracing system. It allows the CBISs with the same inerter to realize an optimal vertical distribution, facilitating the manufacture and deployment of the inerter system.
- The effective inerter-mass ratio reflecting the influence of the installation location and layout of the CBIS on the inerter system's utilization efficiency is used to explain the CICBIS's high efficiency.

It provides a reference for the further optimization of the installation location and layout of the inerter system.

Although the discussion herein is limited to the shear-type structure and some existing cable-bracing systems, based on the tension-only characteristics and flexibility of the cable, it is foreseeable that entirely using these properties will make the application of the CICBIS more prominent. The discussions on the efficiency of the CICBIS equipped in the structures other than shear-type, and the experimental verifications will be carried out in subsequent studies.

Author Contributions: Conceptualization, S.X. and L.X.; methodology, J.K.; software, J.K. and X.B.; validation, J.K. and X.B.; formal analysis, J.K.; writing—original draft preparation, J.K.; writing—review and editing, R.Z., S.X. and L.X. All authors have read and agreed to the published version of the manuscript.

Funding: This research was funded by the National Natural Science Foundation of China (Grant No.51778490 and 51978525), Open Research Fund Program of Guangdong Key Laboratory of Earthquake Engineering and Application Technology (Grant No. 2017B030314068), the Natural Science Foundation of Shanghai (Grant No. 20ZR1461800).

Conflicts of Interest: The authors declare no conflict of interest.

Appendix A

Table A1. Nomenclature list.

Symbol	Parameter Definition
TVMD	tuned viscous mass damper
SDOF	single-degree-of-freedom
MDOF	multiple-degree-of-freedom
TID	tuned inerter damper
CBIS	cable-bracing inerter system
CICBIS	cross-layer installed CBIS
IICBIS	inter-layer installed CBIS
RMS	root mean square
FRF	frequency response function
F_{in}	resisting force of the inerter
u_1, u_2	displacement of the inerter two ends
m_{in}, c_{in}, k_{in}	apparent mass, damping coefficient, and tuning spring stiffness of the TVMD
F_{is}	resisting force of the TVMD
u_{is}, u_d	displacement differences at two ends of the TVMD and the inerter
k_c	cable stiffness
E_c, A_c	elastic modulus and cross-section area of the cable
l_c	cable equivalent length
l_{c1}, l_{c2}	one-side diagonal and horizontal cable length
α	cable installation angle
η	lever arm ratio
γ	seesaw angle
k_s	stiffness of the CBIS
β	displacement transition ratio
m, k, c	mass, stiffness, and damping coefficient of the SDOF structure
$F_{control}$	control force applied to the structure
u_0	ground motion displacement
u	displacement of the structure relative to the ground
u_e	equivalent inerter displacement
m_e, c_e, k_e	equivalent apparent mass, damping coefficient, and stiffness of the CBIS
$x_{p,i}$	relative displacement of the i th layer of the primary structure
$m_{p,i}, k_{p,i}, c_{p,i}$	mass, stiffness, and damping coefficient of the i th layer of the primary structure
n	number of MDOF structure layers
$m_{e,i}, k_{e,i}, c_{e,i}$	equivalent apparent mass, stiffness, and of damping coefficient the i th CBIS

Table A1. Cont.

Symbol	Parameter Definition
$x_{e,i}$	equivalent inerter displacement of the i th CBIS
n_d	total number of the CBIS
α_p	generalized coordinates of the primary structure
α_d	generalized coordinates of the inerter
E_T, E_U, E_D	kinetic energy, strain energy, and dissipated energy of the CBIS equipped n-DOF structure
M_p	generalized mass of the primary structure
M_d	generalized apparent mass of the CBIS
μ	effective inerter-mass ratio
ω_g, ζ_g	frequency property and damping property of the supporting ground
S_0	intensity of the white noise excitation at the bedrock
w	white noise input
σ_u	RMS structural responses
σ_F	RMS control forces
m_d, c_d	designed apparent mass and damping coefficient of the inerter system
β_i	displacement transition ratio of the i th cable-bracing systems
$\omega_r = \sqrt{\frac{k_d}{m_d}}$	frequency of the CBIS
k_d	designed stiffness of the CBISs
J_p	drift reduction ratio
$\sigma_u(i)$	i th RMS story drift of the controlled structure
h_i	i th floor height of the structure
θ_{0max}	maximum RMS story drift ratio of the uncontrolled structure
J_F	cost index of installing n_d CBISs
$\sigma_F(i)$	RMS control force of the i th CBIS
${}_1\omega_0$	natural frequency of the uncontrolled structure
${}_1\mu$	first-order effective inerter-mass ratio
${}_1\phi$	first-order modal vector
J_{target}	target drift reduction ratio

References

- Mahmoodi, P. Structural dampers. *J. Struct. Div.* **1969**, *95*, 1661–1672.
- Housner, G.; Bergman, L.A.; Caughey, T.K.; Chassiakos, A.G.; Claus, R.O.; Masri, S.F.; Skelton, R.E.; Soong, T.; Spencer, B.; Yao, J.T. Structural control: Past, present, and future. *J. Eng. Mech.* **1997**, *123*, 897–971. [\[CrossRef\]](#)
- Yao, J. Concept of structural control. *J. Struct. Div.* **1972**, *98*, 1567–1574.
- Kawamata, S. Accelerated Liquid Mass Dampers as Tools of Structural Vibration Control. In Proceedings of the 9th World Conference on Earthquake Engineering, Tokyo-Kyoto, Japan, 2–9 August 1988; Volume 8, pp. 421–426.
- Ikago, K.; Saito, K.; Inoue, N. Seismic control of single-degree-of-freedom structure using tuned viscous mass damper. *Earthq. Eng. Struct. Dyn.* **2012**, *41*, 453–474. [\[CrossRef\]](#)
- Lazar, I.F.; Neild, S.A.; Wagg, D.J. Using an inerter-based device for structural vibration suppression. *Earthq. Eng. Struct. Dyn.* **2014**, *43*, 1129–1147. [\[CrossRef\]](#)
- Taflanidis, A.A.; Giaralis, A.; Patsialis, D. Multi-objective optimal design of inerter-based vibration absorbers for earthquake protection of multi-storey building structures. *J. Frankl. Inst.* **2019**, *356*, 7754–7784. [\[CrossRef\]](#)
- De Domenico, D.; Ricciardi, G.; Zhang, R. Optimal design and seismic performance of tuned fluid inerter applied to structures with friction pendulum isolators. *Soil Dyn. Earthq. Eng.* **2020**, *132*, 106099. [\[CrossRef\]](#)
- Zhao, Z.; Zhang, R.; Jiang, Y.; De Domenico, D.; Pan, C. Displacement-Dependent Damping Inerter System for Seismic Response Control. *Appl. Sci.* **2020**, *10*, 257. [\[CrossRef\]](#)
- Kawamata, S. *Development of a Vibration Control System of Structures by Means of Mass Pumps*; Institute of Industrial Science, University of Tokyo: Tokyo, Japan, 1973.
- Arakaki, T.; Kuroda, H.; Arima, F.; Inoue, Y.; Baba, K. Development of seismic devices applied to ball screw. Part 1: Basic performance test of RD-series. *AII J. Technol. Des.* **1999**, *5*, 239–244. [\[CrossRef\]](#)
- Arakaki, T.; Kuroda, H.; Arima, F.; Inoue, Y.; Baba, K. Development of seismic devices applied to ball screw: Part 2 Performance test and evaluation of RD-series. *AII J. Technol. Des.* **1999**, *9*, 265–270. [\[CrossRef\]](#)

13. Saito, K.; Sugimura, Y.; Inoue, N. A study on response control of a structure using viscous damper with inertial mass. *J. Struct. Eng.* **2008**, *54*, 623–648.
14. Arai, T.; Aburakawa, T.; Ikago, K.; Hori, N.; Inoue, N. Verification on effectiveness of a tuned viscous mass damper and its applicability to non-linear structural systems. *J. Struct. Constr. Eng. AIJ* **2009**, *645*, 1993–2002. [[CrossRef](#)]
15. Pan, C.; Zhang, R. Design of structure with inerter system based on stochastic response mitigation ratio. *Struct. Control Health Monit.* **2018**, *25*, e2169. [[CrossRef](#)]
16. Pan, C.; Zhang, R.; Luo, H.; Li, C.; Shen, H. Demand-based optimal design of oscillator with parallel-layout viscous inerter damper. *Struct. Control Health Monit.* **2018**, *25*, e2051. [[CrossRef](#)]
17. Shen, W.; Niyitangamahoro, A.; Feng, Z.; Zhu, H. Tuned inerter dampers for civil structures subjected to earthquake ground motions: Optimum design and seismic performance. *Eng. Struct.* **2019**, *198*, 109470. [[CrossRef](#)]
18. Zhang, S.Y.; Li, Y.-Y.; Jiang, J.Z.; Neild, S.A.; Macdonald, J.H.G. A methodology for identifying optimum vibration absorbers with a reaction mass. *Proc. R. Soc. A Math. Phys. Eng. Sci.* **2019**, *475*, 20190232. [[CrossRef](#)]
19. Zhang, R.; Zhao, Z.; Pan, C.; Ikago, K.; Xue, S. Damping enhancement principle of inerter system. *Struct. Control Health Monit.* **2020**, e2523. [[CrossRef](#)]
20. Marian, L.; Giaralis, A. Optimal design of a novel tuned mass-damper–inerter (TMDI) passive vibration control configuration for stochastically support-excited structural systems. *Probabilistic Eng. Mech.* **2014**, *38*, 156–164. [[CrossRef](#)]
21. Giaralis, A.; Marian, L. Use of inerter devices for weight reduction of tuned mass-dampers for seismic protection of multi-story building: The Tuned Mass-Damper-Inerter (TMDI). In *Active and Passive Smart Structures and Integrated Systems*; International Society for Optics and Photonics: Las Vegas, NA, USA, 2016; p. 97991G.
22. Giaralis, A.; Taflanidis, A. Optimal tuned mass-damper-inerter (TMDI) design for seismically excited MDOF structures with model uncertainties based on reliability criteria. *Struct. Control Health Monit.* **2018**, *25*, e2082. [[CrossRef](#)]
23. Garrido, H.; Curadelli, O.; Ambrosini, D. Improvement of tuned mass damper by using rotational inertia through tuned viscous mass damper. *Eng. Struct.* **2013**, *56*, 2149–2153. [[CrossRef](#)]
24. De Domenico, D.; Ricciardi, G. Improving the dynamic performance of base-isolated structures via tuned mass damper and inerter devices: A comparative study. *Struct. Control Health Monit.* **2018**, *25*, e2234. [[CrossRef](#)]
25. De Domenico, D.; Ricciardi, G. An enhanced base isolation system equipped with optimal tuned mass damper inerter (TMDI). *Earthq. Eng. Struct. Dyn.* **2018**, *47*, 1169–1192. [[CrossRef](#)]
26. Angelis, M.; Giaralis, A.; Petrini, F.; Pietrosanti, D. Optimal tuning and assessment of inertial dampers with grounded inerter for vibration control of seismically excited base-isolated systems. *Eng. Struct.* **2019**, *196*. [[CrossRef](#)]
27. Ikago, K.; Sugimura, Y.; Saito, K.; Inoue, N. Seismic displacement control of multiple-degree-of-freedom structures using tuned viscous mass dampers system. In Proceedings of the 8th International Conference on Structural Dynamics EUROSDYN, Leuven, Belgium, 4–6 July 2011; Volume 7, pp. 1800–1807.
28. Ikago, K.; Sugimura, Y.; Saito, K.; Inoue, N. Simple design method for a tuned viscous mass damper seismic control system. In Proceedings of the 15th World Conference on Earthquake Engineering, Lisbon, Portugal, 24–28 September 2012; Volume 9.
29. Wen, Y.; Chen, Z.; Hua, X. Design and evaluation of tuned inerter-based dampers for the seismic control of MDOF structures. *J. Struct. Eng.* **2017**, *143*, 04016207. [[CrossRef](#)]
30. Zhang, S.Y.; Jiang, J.Z.; Neild, S. Optimal configurations for a linear vibration suppression device in a multi-storey building. *Struct. Control Health Monit.* **2017**, *24*, e1887. [[CrossRef](#)]
31. Asai, T.; Watanabe, Y. Outrigger tuned inertial mass electromagnetic transducers for high-rise buildings subject to long period earthquakes. *Eng. Struct.* **2017**, *153*, 404–410. [[CrossRef](#)]
32. Ogino, M.; Sumiyama, T. Structural design of a high-rise building using tuned viscous mass dampers installed across three consecutive storeys. In Proceedings of the Twelfth International Conference on Computational Structures Technology, Naples, Italy, 2–5 September 2014.
33. Hwang, J.-S.; Kim, J.; Kim, Y.-M. Rotational inertia dampers with toggle bracing for vibration control of a building structure. *Eng. Struct.* **2007**, *29*, 1201–1208. [[CrossRef](#)]

34. Xie, L.; Ban, X.; Xue, S.; Ikago, K.; Kang, J.; Tang, H. Theoretical Study on a Cable-Bracing Inerter System for Seismic Mitigation. *Appl. Sci.* **2019**, *9*, 4096. [[CrossRef](#)]
35. Sorace, S.; Terenzi, G. The damped cable system for seismic protection of frame structures—Part I: General concepts, testing and modeling. *Earthq. Eng. Struct. Dyn.* **2012**, *41*, 915–928. [[CrossRef](#)]
36. Sorace, S.; Terenzi, G. The damped cable system for seismic protection of frame structures—Part II: Design and application. *Earthq. Eng. Struct. Dyn.* **2012**, *41*, 929–947. [[CrossRef](#)]
37. Aly, A.M. The Use of Bracing Systems with MR Dampers in Super Tall Buildings. *Int. J. High Rise Build.* **2016**, *5*, 31–41. [[CrossRef](#)]
38. Kang, J.-D.; Tagawa, H. Seismic performance of steel structures with seesaw energy dissipation system using fluid viscous dampers. *Eng. Struct.* **2013**, *56*, 431–442. [[CrossRef](#)]
39. Sugimura, Y.; Goto, W.; Tanizawa, H.; Saito, K.; Nimomiya, T. Response control effect of steel building structure using tuned viscous mass damper. In Proceedings of the 15th World Conference on Earthquake Engineering, Lisbon, Portugal, 24–28 September 2012; Volume 9, pp. 24–28.
40. Lutes, L.D.; Sarkani, S. *Random Vibrations: Analysis of Structural and Mechanical Systems*; Butterworth-Heinemann: Oxford, UK, 2004.
41. Kanai, K. Semi-empirical formula for the seismic characteristics of the ground. *Bull. Earthq. Res. Inst. Univ. Tokyo* **1957**, *35*, 309–325.
42. JSSI Manual. *Design and Construction Manual for Passively Controlled Buildings*, 2nd ed.; Japan Society of Seismic Isolation: Tokyo, Japan, 2005. (In Japanese)



© 2020 by the authors. Licensee MDPI, Basel, Switzerland. This article is an open access article distributed under the terms and conditions of the Creative Commons Attribution (CC BY) license (<http://creativecommons.org/licenses/by/4.0/>).